Entrainment in variable-density jets

P. Salizzoni[1,2]†, S. Vaux[3], M. Creyssels[1], J. Craske[4] and M. van Reeuwijk[4]

[1]Laboratoire de Mécanique des Fluides et d'Acoustique, University of Lyon, CNRS UMR 5509 Ecole Centrale de Lyon, INSA Lyon, Université Claude Bernard, 36, avenue Guy de Collongue, 69134 Ecully, France.

[2]Department of Environmental, Land, and Infrastructure Engineering, Politecnico di Torino, Corso Duca degli Abruzzi 24, 10129 Turin, Italy

[3]Institut de Radioprotection et de Sûreté Nucléaire, PSN-RES, SA2I, LIE, Cadarache, 13115 St Paul-Lez-Durance, France.

[4]Department of Civil and Environmental Engineering, Imperial College London, Imperial College Road, London SW7 2AZ, UK.

(Received 27 September 2024)

The entrainment of ambient fluid into a variable-density jet is typically quantified using an entrainment coefficient α. Here, we investigate the dependence of α on the ratio of the jet's density ρ_m and that of the ambient fluid ρ_0. Current parametrisations of α rely on a scaling inferred from early laboratory experiments (Ricou & Spalding, *J. Fluid Mech.*, vol. 11, 1961, pp. 21-32). We demonstrate analytically that the experiments preclude definitive conclusions regarding the dependence of α on ρ_m/ρ_0 and that the underlying physical processes therefore warrant closer attention. To investigate the physics behind the dependence of entrainment on the density ratio we use a Favre-averaged entrainment decomposition. The decomposition is applied to data from large-eddy simulations (LES) of jets characterised by density ratios ρ_m/ρ_0 spanning over two orders of magnitude that have been verified against experimental data. Changes in the shape of the velocity profile are a significant contributor to entrainment in the near field due to the breakdown of the potential core, and persist over larger streamwise distances in heavy releases than in light releases. Therefore, to focus exclusively on the effects of density ratio, we study the region where the shape changes have become small but the density ratio is still significant. We show that the dimensionless turbulent kinetic energy production and mean kinetic energy flux depend strongly on the density ratio, both for our LES data and for recent experiments. Despite this, the entrainment coefficient is practically constant in this region and has value $\alpha \approx 0.07$ for all simulations.

1. Introduction

A variable-density jet is a flow induced by the continuous release of a fluid of density ρ_s from a circular source, of radius r_s at a steady uniform velocity w_s within a still environment of density ρ_0. For sufficiently high Reynolds number $Re_s = w_s r_s/\nu_s$ (ν_s is the kinematic viscosity of the fluid discharged) the flow is fully turbulent, and the growth of inertial instabilities give rise to complex and multiscale dynamics (see figure 1). The process leads to the entrainment of ambient fluid within the jet that ultimately results in the mixing and dilution of the discharged fluid. These releases are referred to

† Email address for correspondence: pietro.salizzoni@ec-lyon.fr

as jets (instead of plumes or fountains) because their dynamics are momentum (rather than buoyancy) dominated, which implies that their Richardson number at the source $Ri_s = \dfrac{gr_s(\rho_s - \rho_0)/\rho_0}{w_s^2} \to 0$. We can therefore assume that gravitational effects are negligible in the flow dynamics.

Examples of variable-density turbulent jets (and plumes) can be found in several areas of engineering and the physical sciences, e.g. ocean outfalls, exhausts of engines, volcanic eruptions, releases of chemicals from pipes and reservoirs. A robust approach in the modelling of these flows is provided by the plume equations (see, e.g. Priestley & Ball 1955; Morton *et al.* 1956), which provide an integral description of the flow, in which spatially averaged variables depend only on the distance from the source z (figure 1). In this framework, the integration of the equation of conservation of (time-averaged) mass over the radial coordinate r (see figure 1), leads to:

$$\frac{\mathrm{d}G}{\mathrm{d}z} = 2\rho_0 \alpha w_m r_m, \tag{1.1}$$

where $G \equiv 2\int_0^\infty \overline{\rho w} r \mathrm{d}r$ is the time-averaged mass flux (w is the jet velocity along the streamwise direction z, ρ is the jet density and overbar denotes Reynolds averages), α is the entrainment coefficient, and r_m and w_m are characteristic scales of the jet width and velocity, respectively (their definition is given in §2).

Our focus is the parameter α, controlling the dilution of the jet with the ambient fluid. A reference study providing experimental measurements of the entrainment process within variable-density releases is that of Ricou & Spalding (1961), hereafter referred to as R&S. Their results suggest a dependence of α on a local jet density scale $\rho_m(z)$ (also defined in §2), and a scaling of the form

$$\alpha = \alpha_0 \left(\frac{\rho_m}{\rho_0}\right)^\beta, \tag{1.2}$$

with $\beta = 1/2$ and α_0 the entrainment coefficient for a pure (iso-density) jet, which they set equal to 0.08, which is slightly larger than that estimated in other studies (Papanicolaou & List 1988; Wang & Law 2002; Ezzamel *et al.* 2015; van Reeuwijk *et al.* 2016). According to (1.2), the rate of dilution of the jet is therefore increased for an increasing density ratio ρ_m/ρ_0. This result was subsequently interpreted physically by Morton (1965) in terms of the influence of the Reynolds stress (i.e. of the turbulent kinetic energy (TKE) production) on the entrainment process. Almost forty years after the seminal work by R&S, Rooney & Linden (1996) and Woods (1997) adopted an entrainment parameterisation on the basis of (1.2) with $\beta = 1/2$, showing that the dynamics of a so-called non-Boussinesq plume (i.e. characterised by large density variations between plume and ambient fluid) could be ultimately modelled in analogy with the classical plume theory. This led to the adoption of self-similar solutions for non-Boussinesq plumes (Van den Bremer & Hunt 2010), that could be subsequently applied to releases in unconfined and confined environments (Vauquelin 2015; Jiang *et al.* 2019; Mehaddi *et al.* 2021).

R&S's variable-density jets have been studied using experiments (see, e.g. Panchapakesan & Lumley 1993; Gharbi *et al.* 1995; Amielh *et al.* 1996; Djeridane *et al.* 1996; Pietri *et al.* 2000; O'Hern *et al.* 2005; Ai *et al.* 2006; Gerashchenko & Prestridge 2015; Charonko & Prestridge 2017; Viggiano *et al.* 2018) and numerical simulations (see, e.g. Gharbi *et al.* 1996; García-Villalba *et al.* 2006; Wang *et al.* 2008). However, the determination of the dependence of the entrainment coefficient on the density ratio was however beyond the

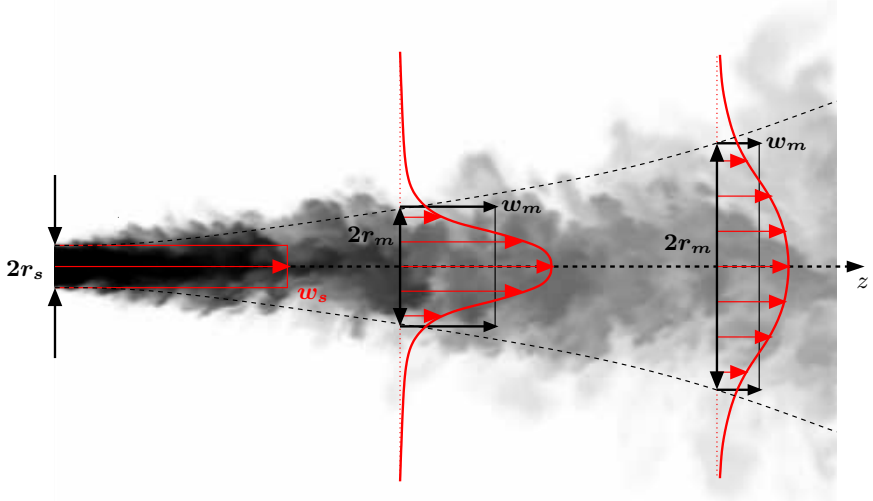


FIGURE 1. Instantaneous density ratio ρ_m/ρ_0 of a turbulent jet with $\rho_s/\rho_0 = 0.2$ (large-eddy simulation): white corresponds to $\rho/\rho_0 = 1$ while black to $\rho/\rho_0 = 0.2$. Superimposed are the averaged value of the streamwise velocity (in red), the top-hat velocity w_m and the radius r_m at varying axial distance z from the source.

scope of these studies. None, therefore, could confirm (or invalidate) the scaling provided by (1.2).

The issue was tackled recently by Salizzoni *et al.* (2023), who estimated velocity and density statistics within a low-density jet ($\rho_m/\rho_0 = 0.4$) and an iso-density jet by means of laboratory experiments and large-eddy simulations. Their results highlight the role of a reduced density on the jet dynamics, notably by enhancing the TKE production and modifying the shape of the mean streamwise velocity. Despite this, their results clearly indicate that a reduced density has no major effect in modifying the entrainment coefficient α, whose evolution for increasing distance from the source does not differ significantly from that observed in an iso-density jet (therefore contradicting the R&S scaling). The aim of this study is to build upon the recent results by Salizzoni *et al.* (2023) and extend their analysis to a broader set of source density conditions (ρ_s), carrying out an exhaustive investigation into the dependence of flow dynamics and the entrainment process in variable-density jets.

We begin by revisiting the scaling (1.2) proposed by R&S, showing analytically that their experimental results are not conclusive in determining the value of the exponent β. We then present the details of the large-eddy simulations (§4) of jets with varying density ratios (spanning over two orders of magnitude) and the entrainment decomposition (§3), which we subsequently use to interpret the numerical results. Next, we analyze the evolution of integral quantities characterizing the entrainment dynamics, integrating in our discussion the evidence provided by recent experimental data on light (Salizzoni *et al.* 2023) and heavy (Charonko & Prestridge 2017) jets, and ultimately investigate the dependence of α on the density ratio (§5).

2. Revisiting the experimental results of Ricou and Spalding

By employing a meticulous experimental approach, Ricou & Spalding (1961) successfully estimated the entrained ambient air flux within a variable-density jet. This estimation was achieved using a porous screen positioned at the jet border, therefore avoiding challenging (especially at that time) measurements of local fluid velocities and densities

within the jet. Their conclusion was that the mass fluxes G of the different releases, normalised by their source value G_s, collapsed when plotted against vertical coordinate rescaled on $(\rho_s/\rho_0)^{-1/2}$ (see figure 2*c-d*). Coupled with the assumption of a constant momentum flux, corresponding to negligible gravitational effects on the flow dynamics, their results led to the conclusion that $\beta = 1/2$ in (1.2).

In this section we demonstrate that the experiments of R&S do not provide sufficient information to determine the exponent β in (1.2) because, to leading order, the value of β does not affect the scaling og G in the far field.

To show this, we solve (1.1) analytically, assuming that α scales as (1.2) without specifying β. We then compare solutions for two values of β in the near field ($z/r_s \leq 30$, figure 2*a-b*), where variable density effects are large, and in the far field (z/r_s up to 900). The latter range was investigated by R&S (figure 2*c-d*), which allows for a direct comparison between the analytical solution and their data.

In what follows, the characteristic velocity, radius and density of the jet are defined as $w_m = M/G$, $r_m = (QG/M)^{1/2}$, and $\rho_m = G/Q$, respectively, as a function of the mass G, volume Q and momentum M fluxes (Salizzoni *et al.* 2023). Adopting Favre averages (denoted by a tilde and defined as $\widetilde{\chi} = \overline{\chi\rho}/\overline{\rho}$) the fluxes are expressed as $G = 2\int_0^\infty \overline{\rho}\widetilde{w}r\mathrm{d}r = \rho_m w_m r_m^2$, $Q = 2\int_0^\infty \widetilde{w}r\mathrm{d}r = w_m r_m^2$, and $M = 2\int_0^\infty \overline{\rho}\widetilde{w}^2 r\mathrm{d}r = \rho_m (w_m r_m)^2$.

2.1. *Analytical solutions for the mass flux G*

Since we are assuming negligible buoyancy effects, which means that the momentum flux is conserved, i.e. $M \equiv \rho_m w_m^2 r_m^2 = \rho_s w_s^2 r_s^2$, (with $r_s = r_m(z=0)$, $w_s = w_m(z=0)$ and $\rho_s = \rho_m(z=0)$), the mass balance equation (1.1) can be rewritten as

$$\frac{\mathrm{d}(G/G_s)}{\mathrm{d}(z/r_s)} = 2\alpha \left(\frac{\rho_m}{\rho_0}\right)^{-1/2} \left(\frac{\rho_s}{\rho_0}\right)^{-1/2}. \tag{2.1}$$

By further assuming a low-Mach number flow at high Reynolds number (i.e. negligible viscous effects) it can be shown (Rooney & Linden 1996) that the flow has a divergence-free velocity field, which, in turn, implies that the density deficit flux is conserved, such that $(\rho_0 - \rho_m) w_m r_m^2 = (\rho_0 - \rho_s) w_s r_s^2$, or, expressed in terms of G,

$$\frac{\rho_0}{\rho_m} = 1 + \Delta_s \frac{G_s}{G}, \tag{2.2}$$

where $\Delta_s = (\rho_0 - \rho_s)/\rho_s$ and $G_s = \rho_s w_s r_s^2$. Combining (2.1) and (2.2), and assuming that α exhibits a power-law dependence of the form (1.2), leads to

$$\frac{\mathrm{d}(G/G_s)}{\mathrm{d}(z/r_s)} = 2\alpha_0 \left(\frac{\rho_s}{\rho_0}\right)^{-1/2} \left[1 + \Delta_s \frac{G_s}{G}\right]^{1/2-\beta}. \tag{2.3}$$

For $\beta = 1/2$, integrating (2.3) gives:

$$\frac{G}{G_s} = 1 + 2\alpha_0 \left(\frac{\rho_s}{\rho_0}\right)^{-1/2} \frac{z}{r_s}, \text{ for } \beta = 1/2, \tag{2.4}$$

which is the reference relation used by R&S to rescale their experimental results and demonstrate collapse onto a single non-dimensional curve. Indeed, (2.4) exhibits a dependence on the source conditions (r_s and ρ_s) only, and not on the local jet radius r_m, density ρ_m or velocity w_m, which R&S werenot able to measure using their experimental apparatus.

When considering the general case of $\beta \neq 1/2$, G/G_s is not linear in z/r_s and therefore does not scale with $(\rho_s/\rho_0)^{-1/2}$. However, we show hereafter that, irrespective of the β value, G/G_s behaves as $(\rho_s/\rho_0)^{-1/2}\frac{z}{r_s}$ at large distances from the source, i.e. $z \gg r_s$, corresponding to the limit $G_s/G \to 0$. By defining $\epsilon = G_s/G$, the differential equation for ϵ is

$$\frac{\mathrm{d}\epsilon}{\mathrm{d}(z/r_s)} + 2\alpha_0 \left(\frac{\rho_s}{\rho_0}\right)^{-1/2} \epsilon^2 \left[1 + \Delta_s \epsilon\right]^{-\gamma} = 0, \tag{2.5}$$

with $\gamma = \beta - 1/2$. Separating ϵ and z/r_s and integrating leads to

$$\int_\epsilon^1 \left[1 + \Delta_s x\right]^\gamma \frac{\mathrm{d}x}{x^2} = 2\alpha_0 \left(\frac{\rho_s}{\rho_0}\right)^{-1/2} \frac{z}{r_s}. \tag{2.6}$$

Formally, the integrand of the left-hand side of (2.6) can be expanded as a power series which can be integrated term by term:

$$\int_\epsilon^1 \left[1 + \Delta_s x\right]^\gamma \frac{\mathrm{d}x}{x^2} = \int_\epsilon^1 \left[1 + \sum_{n=1}^{\infty} \binom{\gamma}{n} (\Delta_s x)^n\right] \frac{\mathrm{d}x}{x^2} \tag{2.7}$$

$$= \frac{1}{\epsilon} - 1 - \gamma\Delta_s \ln\epsilon + \sum_{n=2}^{\infty} \binom{\gamma}{n} \frac{(\Delta_s)^n}{n-1} \left(1 - \epsilon^{n-1}\right). \tag{2.8}$$

At large distances from the source, $\epsilon = G_s/G \to 0$ the leading-order contribution from (2.8) is $1/\epsilon = G/G_s$ which from (2.6) implies that

$$\frac{G}{G_s} \sim 2\alpha_0 \left(\frac{\rho_s}{\rho_0}\right)^{-1/2} \frac{z}{r_s}, \text{ for any } \beta \text{ with } G_s/G \to 0. \tag{2.9}$$

This limit can be easily confounded with the exact solution for $\beta = 1/2$ (2.4). In other words, when performing measurements in the far field where $G/G_s \gg 1$, we expect G/G_s to scale with $(\rho_s/\rho_0)^{-1/2}$ *regardless* of the value of the exponent β.

2.2. *Near- and far-field behaviour and comparison with R&S data*

In order to analyse the dependence of the mass flux G on the exponent β, we focus on the near-field region, i.e. $z/r_s \leq 30$ (for which R&S did not obtain data), and compare the R&S model ($\beta = 1/2$, Eq. (2.4)) and solution of the differential equation (2.3) with $\beta = 0$. The results are plotted in figure 2(a) for the three density ratios investigated by R&S: $\rho_s/\rho_0 = 1.5$ (carbon dioxide in air), $\rho_s/\rho_0 = 1$ (air in air), and $\rho_s/\rho_0 = 0.069$ (hydrogen in air).

The results, plotted in figure 2(a), show that, for density ratios slightly different than unity (i.e. the carbon dioxide release), the value of β has very little effect on the mass flux $G(z)/G_s$. Significant differences can instead be seen for the case of hydrogen, for which the two solutions ($\beta = 0$ and $\beta = 1/2$) lead to differences of almost 50% after few source radii from the source. Consequently, the different solutions do not collapse on a single curve, when re-scaling the data as in R&S (figure 2(b)).

Turning to the far field, and including R&S data in our analysis, we obtain a different picture (see figures 2 (c) and (d)). As previously pointed out, the solutions obtained for the two different β are almost indistinguishable when plotted over large distances from the source, i.e. up to $z/r_s = 900$. Therefore, very good agreement is observed between the experimental data and both analytical solutions, one obtained using the R&S model ($\beta = 1/2$, dotted lines) and the other using an entrainment coefficient that is independent of the density ratio ($\beta = 0$, dashed lines). Both solutions collapse, as a first

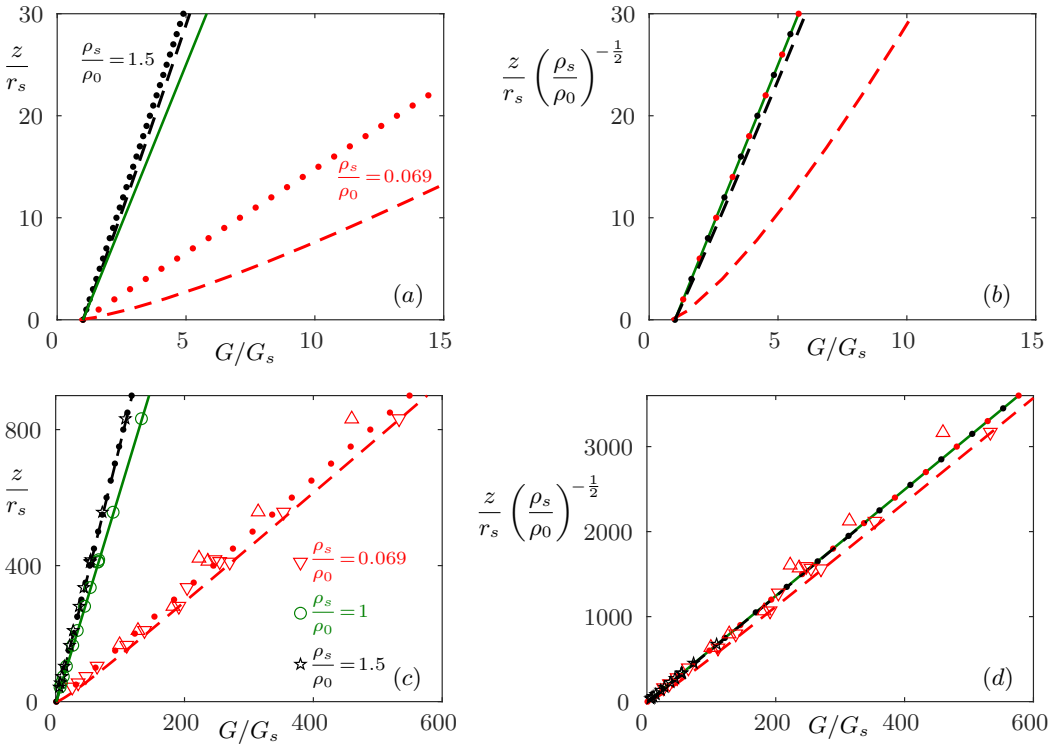


FIGURE 2. Results of analytical solutions for $z/r_s \leq 30$ $(a-b)$ and for $z/r_s \leq 900$ $(c-d)$. Dotted lines: R&S model, $\beta = 1/2$, Eq. (2.4) for $\rho_s/\rho_0 = 0.069$ (in red) and for $\rho_s/\rho_0 = 1.5$ (in black). Solid green line: (2.4) with $\rho_s = \rho_0$. Dashed lines: solution of the differential equation (2.3) with $\alpha = \alpha_0 = 0.08$, the value originally used by R&S (see text), and $\beta = 0$. Experimental results of Ricou & Spalding (1961) are also shown in $(c-d)$ (symbols).

approximation, on a single curve. Indeed, the discrepancies between the two solutions in figures 2(d) are lower than the uncertainties observed in the experimental data.

We conclude that the solution of the differential equation (2.3) is sensitive to the value of β in the near-field but not in the far-field. Therefore, the collapse of the experimental data on a single curve in the far-field according to (2.9), as observed by R&S, does not imply that the entrainment coefficient scales as (1.2), with $\beta = 1/2$.

3. The entrainment relation

Based on early work of Priestley & Ball (1955), recent studies (Kaminski *et al.* 2005; van Reeuwijk & Craske 2015; Ezzamel *et al.* 2015; Craske *et al.* 2017) on isodensity jets and Boussinesq plumes have shown that, by combining the mass, momentum and mean kinetic energy balance equations, a relation for the entrainment coefficient, expressed as a function of local flow statistics, can be obtained. As discussed by Salizzoni *et al.* (2023), this framework can be conveniently extended to the more general case of large density difference between an ambient fluid and the release, by using Favre averages.

To the leading order, the entrainment relation for a momentum-dominated release (in which the role of gravity is negligible) can be written as (Salizzoni *et al.* 2023)

$$\alpha_E = \underbrace{-\frac{\rho_m}{\rho_0}\frac{\delta_m}{2\gamma_m}}_{\alpha_{prod}} + \underbrace{\frac{\rho_m}{\rho_0} r_m \frac{\mathrm{d}}{\mathrm{d}z}\left(\ln \gamma_m^{1/2}\right)}_{\alpha_{shape}}, \tag{3.1}$$

where

$$\gamma_m = \frac{2}{\rho_m w_m^3 r_m^2}\int_0^\infty \overline{\rho}\widetilde{w}^3 r\mathrm{d}r, \qquad \delta_m = \frac{4}{\rho_m w_m^3 r_m}\int_0^\infty \overline{\rho}\widetilde{w''u''}\frac{\partial \overline{w}}{\partial r} r\mathrm{d}r,$$

and double primes denote fluctuations from the Favre averages. The parameters γ_m and δ_m correspond to the dimensionless mean flux and production of kinetic energy, respectively, and are referred to as 'profile coefficients' because their value depends on the radial dependence of the primitive flow variables.

As evidenced by (3.1), the entrainment coefficient is determined by two contributions (both weighted by the ratio between the top-hat jet density ρ_m, varying with the streamwise coordinate, and the ambient density ρ_0): i) α_{prod}, directly linked to the ratio of production of turbulent kinetic energy to the mean kinetic energy flux, and ii) α_{shape}, which depends on the change of the form of the radial profiles of mean streamwise velocity. A priori, there is no reason not to assume a possible dependence of α_{prod} and α_{shape} on ρ_m/ρ_0, which is effectively taken as unity in the far-field and therefore typically ignored.

Note that the estimate of the entrainment coefficient as given by (3.1) is independent from that provided by (1.2), denoted here as α, and linked to the rate of change of the mass flux $G(z)$ for increasing distance from the source. However, to fulfill basic mass, momentum and kinetic energy balances, the coefficients α and α_E have to coincide at any distance from the source.

As also revealed by (3.1), the evolution of the entrainment coefficient can be captured by analysing three main variables of the flow: the mean streamwise velocity $\widetilde{w}$, the Reynolds stress $\widetilde{w''u''}$, and the density $\overline{\rho}$. The determination of these flow statistics by means of laboratory experiments faces practical and metrological difficulties (as discussed in Salizzoni *et al.* 2023), which can be conveniently circumvented by performing numerical simulations.

4. Numerical Simulations

Numerical simulations of variable-density jets in a quiescent environment were performed using the numerical computational code CALIF^{3}S (developed at the Institut de Radioprotection et de Sûreté Nucléaire-IRSN), dedicated to three-dimensional simulations of turbulent and slightly compressible flows (low-Mach-number approach).

The code uses large-eddy simulation to solve the Favre-filtered Navier-Stokes equations (mass and momentum balance), along with species transport equations, in Cartesian coordinates. The subgrid scale Reynolds stresses are modelled by the Vreman subgrid-scale model (Vreman 2004), and a gradient diffusion hypothesis (SGDH) is used to close the problem with a turbulent Schmidt number Sc_t set to 0.7. As molecular viscosity is disregarded in this formalism, the Reynolds number is undefined. The code has been previously used to study flows characterised by large density differences such as light jets (Salizzoni *et al.* 2023) and heavy and light fountains (Vaux *et al.* 2019).

The domain is a cube of size $40\,r_s$, with r_s the jet radius at the source. In the central part of the domain (a rectangular cuboid with square section of side length $10r_s$ centred on the origin) a refined grid size of $r_s/14$ is used. The grid is then progressively stretched for increasing distance from the jet axis, as in Salizzoni *et al.* (2023). In

the vertical direction the grid size is equal to $r_s/8$. For the time discretization, a CFL (Courant-Friedrichs-Lewy) number close to unity has been imposed for each calculation even though time step sizes for which CFL numbers greater than one are allowed with the use of implicit schemes. Each simulation lasted $1000T$ where $T = r_s/w_s$. Results for the first $400T$ were discarded and flow statistics were computed over an interval of $600T$. At the source, the inlet flow was perturbed with the method presented by Jarrin *et al.* (2006) in order to trigger the transition to turbulence. All numerical simulations have been performed with the same computational settings (grid and duration), spatially uniform source conditions and inlet perturbation, except for the density ratio ρ_s/ρ_0.

The source is set flush with the bottom solid boundary of the computational domain from which the jet emerges at the centre with a top-hat inlet mean velocity profile. Since we consider jets in an infinite (open) environment, the computational domain must be bounded by artificial boundary conditions which perturb as little as possible the flow in the interior of the domain. The boundary conditions used in our simulations are based on the control of kinetic energy, allowing one to distinguish between the flow that leaves the domain and the flow that enters it (Bruneau & Fabrie 1994; Bruneau 2000; Bruneau & Fabrie 1996). We have performed eight numerical simulations of turbulent jets (three light releases, four heavy releases and an iso-density jet) with a density ratio ρ_s/ρ_0 spanning over almost two orders of magnitude, i.e. $0.2 \leq \rho_s/\rho_0 \leq 10$. Our experience is that spatially uniform source conditions naturally promote the decay of the potential core, although the difference we observed in supplementary simulations of light jets using spatially non-uniform source conditions did not significantly affect the results.

In order to avoid any effects of variable density associated with the gravitational field (i.e. buoyancy effects), we considered a situation without gravity, by imposing a null gravitational acceleration in the momentum budget. Despite this, we will still refer to as "heavy" the high density releases ($\rho_s > \rho_0$) and the low density releases ($\rho_s < \rho_0$) as "light".

A detailed verification of the reliability of the code in reproducing the first- and second-order flow statistics was performed in Salizzoni *et al.* (2023), who compared the LES simulation with experimental results for an air-helium jet with initial density ratio $\rho_s/\rho_0 = 0.4$ and for an iso-density jet. Their study included an analysis of the effect on the flow statistics of slightly different boundary conditions as well as different sub-grid models. It was shown that the results were not sensitive to the subgrid model and that boundary conditions could impact local flow statistics near the source, but do not significantly affect the integral flow statistics.

5. Results

5.1. *Local and integral flow statistics*

An overview of the results of the eight simulations is provided in figure 3. Here we show the vertical evolution of integral flow variables as a function of the distance from the source. Figure 3*a* presents the variation of the density ratio ρ_m/ρ_0 due to the progressive dilution with the ambient fluid: its decay for heavy releases and its increase for the light ones. This dilution process is accompanied by an enhancement of the jet radius r_m (figure 3*b*), a decay of the jet velocity w_m (figure 3*c*) and an increase of the volume Q and mass G fluxes (figure 3*d*,*e*).

Figure 3*e* demonstrates that the heavier the release, the lower the growth rate of the non-dimensional mass flux G/G_s. Conversely, the non-dimensional volume flux Q/Q_s is higher for heavier releases (figure 3*d*). Indeed, if the entrained fluid has a density which

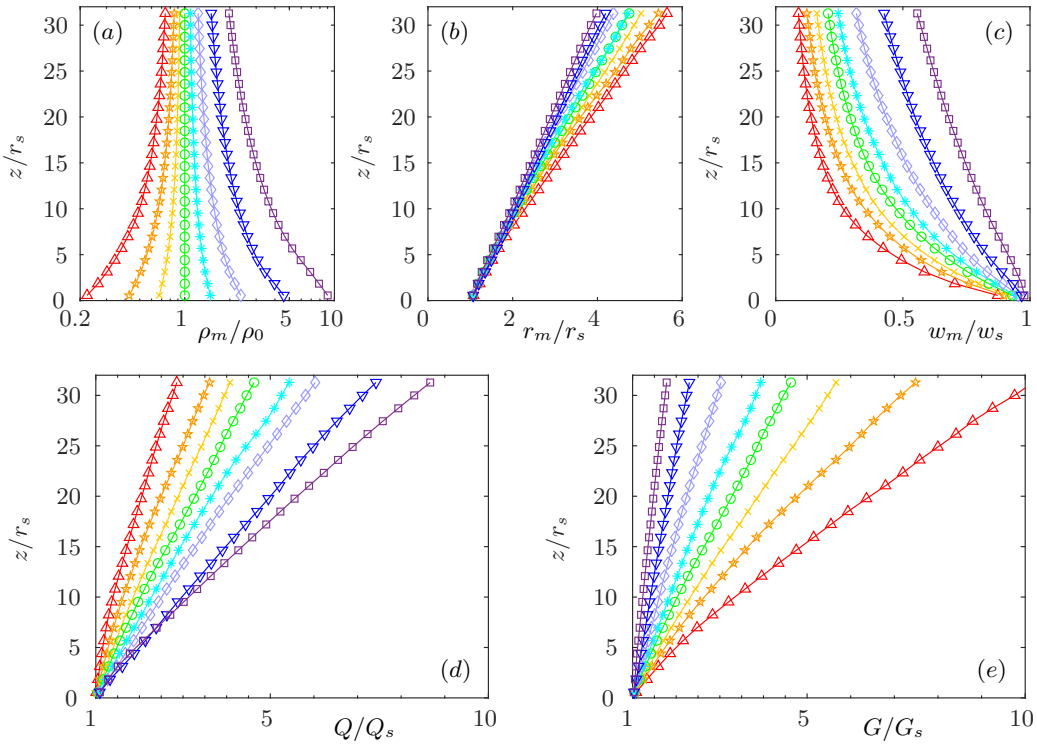


FIGURE 3. Density ratio (a), jet width (b), jet velocity (c), volume (d) and mass (e) fluxes as a function of the streamwise z coordinate. Eight jets have been simulated, from the lightest to the heaviest: $\rho_s/\rho_0 = 0.2$ ($\triangle$), 0.4 ($*$), 0.66 ($\times$), 1 ($\circ$), 1.5 ($\star$), 2.5 ($\diamond$), 5 ($\triangledown$), 10 ($\square$).

is much smaller than the jet density, it contributes little to the enhancement of the mass flux G. These heavy releases dilute more slowly than their lighter counterparts, as is evidenced by a reduced growth rate for the jet radius r_m and a reduced decay of the jet velocity w_m.

As discussed in Section 3, besides the evolution of the jet density ρ_m and the mass flux G, the key elements underlying the turbulent entrainment process (3.1) are the evolutions of the radial profiles of the mean vertical velocity $\widetilde{w}(r,z)$ and of the Reynolds stress $\widetilde{w''u''}(r,z)$. We therefore focus on these two flow variables, whose radial profiles are presented in figure 4, for three of the simulated jets: a light jet ($\rho_s/\rho_0 = 0.2$), the iso-density jet ($\rho_s/\rho_0 = 1$) and a heavy jet ($\rho_s/\rho_0 = 5$). The light jet clearly exhibits a more rapid modification of the radial profiles of both $\widetilde{w}$ and $\widetilde{w''u''}$, compared to the other two (figure4a,d). The uniform conditions imposed at the source are almost immediately lost, even in the core of the jet, for $z/r_s > 5$. Therefore the extent of the potential core tends to be smaller as the density ratio is reduced. Analysing the case of the heavy jet, we can observe a flat velocity profile in the core of the jet that persists up to $z/r_s = 15$ (see figure 4a-c). Corresponding profiles of the Reynolds stress (see figure 4d-f) exhibit zero value in the core of the jet that persists much longer within heavy releases, and one peak that increases in magnitude for the light release.

As a consequence of the behaviour shown in figure 4, the profile coefficients γ_m and δ_m exhibit significant variation (see figure 5a,b). It is worth noting that, since the simulations are characterized by the same boundary conditions at the source, all variations observed in the profile coefficients γ_m and δ_m are solely due to the varying density ratios. In the

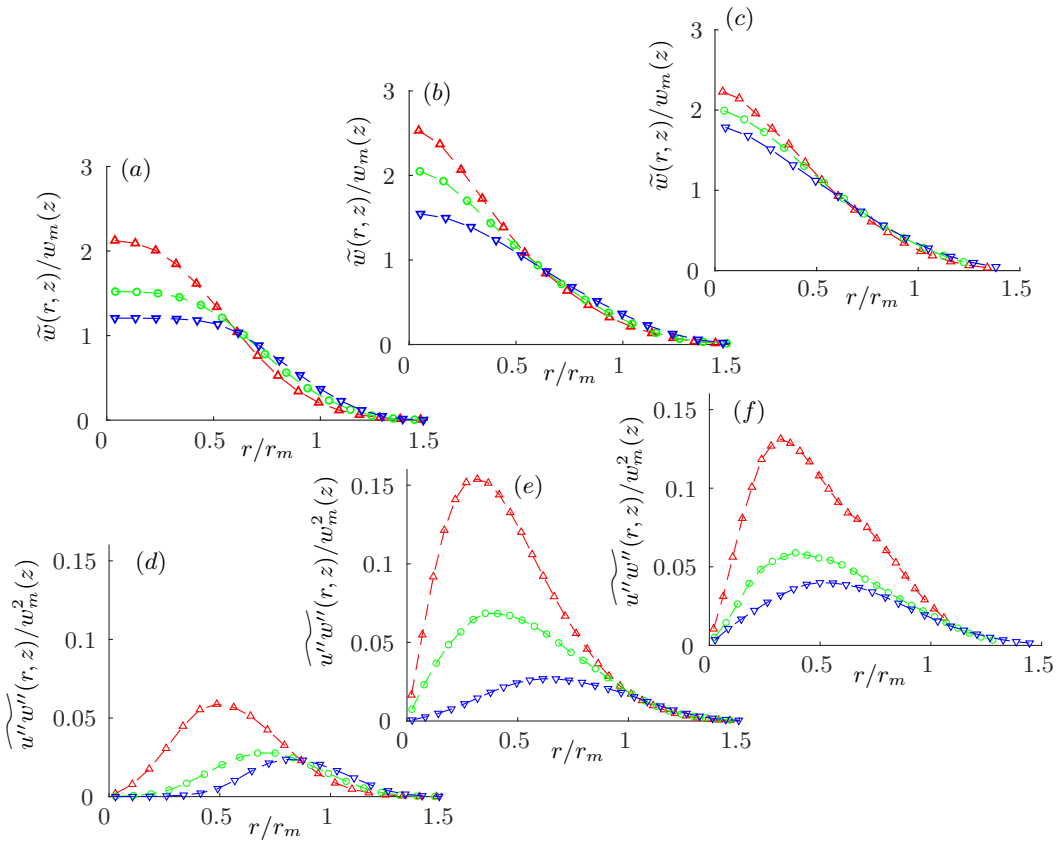


FIGURE 4. Radial profiles of mean vertical velocity $\widetilde{w}$ (*a*,*b*,*c*) and Reynolds stress $\widetilde{u''w''}$ (*d*,*e*,*f*) for a light jet with ($\rho_s/\rho_0 = 0.2$), an iso-density jet and a heavy jet ($\rho_s/\rho_0 = 5$). Symbols as in figure 3. From left to right: $z = 5$, 15 and $30\,r_s$.

case of light releases, the dimensionless mean kinetic energy flux γ_m increases sharply in the near field, exceeding the asymptotic value $\gamma_m = 4/3$, which corresponds to a Gaussian radial velocity profile. Its peak is just below $z/r_s = 10$, after which it reduces in value. The maximum value reached by γ_m depends on the density ratio at the source: the smaller the density ratio, the higher the value of the peak. Conversely, for heavy jets, moving away from the source, the value of γ_m increases smoothly and tends progressively to the asymptotic value for an iso-density jet, which is far from being attained at the top of our computational domains for most of the cases analysed. The larger the density ratio at the source the smoother the increase of γ_m with distance from the source.

The behaviour of the non-dimensional TKE production term $-\delta_m$ is qualitatively similar to that of the dimensionless mean kinetic energy flux term γ_m. For light releases, we observe a rapid increase up to a peak and a subsequent decrease. Heavy releases exhibit instead a progressive enhancement towards the asymptotic value. Physically this means that light jets are characterised by a larger TKE production in the near field, when compared to iso-density jets, and that in heavy jets the TKE production is instead inhibited.

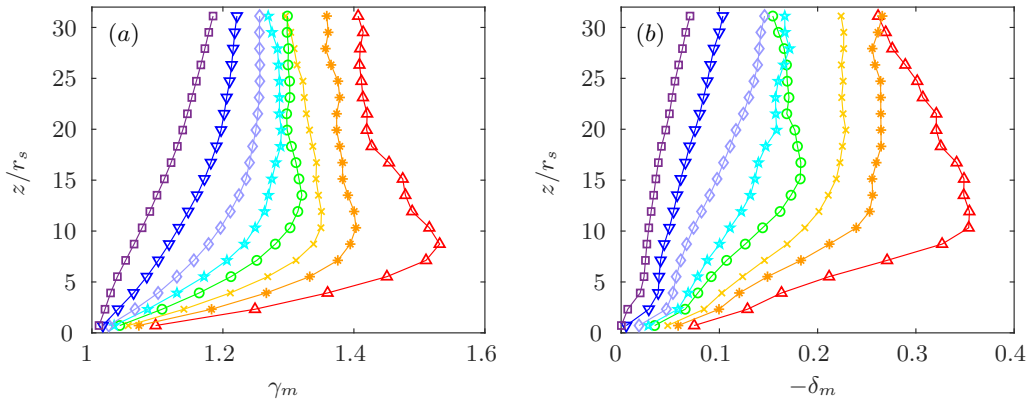


FIGURE 5. Vertical evolution of the (*a*) γ_m (*b*) δ_m profile coefficients. Symbols as in figure 3.

5.2. *Entrainment*

According to (3.1), the variations of γ_m and δ_m, observed for the jets with varying density ratios at the source, are expected to have a direct impact on the entrainment rate. Depending on the initial source conditions, these affect the entrainment coefficient α_E in different ways by inducing variations on both the production and the shape terms ($\alpha_E = \alpha_{prod} + \alpha_{shape}$). Figures 6*a-f* show the evolution with distance from the source of the entrainment coefficients α, as defined by (1.1), and α_E, α_{prod}, α_{shape}, as defined by (3.1) for six (light and heavy) releases.

For all cases the values of the two coefficients α and α_E (represented by solid black lines and filled symbols, respectively, in figure 6*a-d*), which provide independent means of evaluating entrainment, are in good agreement. This means that, as previously observed for Boussinesq plumes (van Reeuwijk *et al.* 2016), neglecting higher order terms is a reasonable approximation for the estimate of α_E (see Salizzoni *et al.* (2023) for further details). The only differences between the two can be observed very close to the source for the two heaviest releases ($\rho_s/\rho_0 = 5; 10$). Figure 6b-c show good agreement with the experimental estimate of α by Salizzoni *et al.* (2023), for the case $\rho_s/\rho_0 = 0.4$ and for the iso-density jet. Further insight on the numerical estimates of the α_{prod} and α_{shape} coefficients (which are not plotted here to limit the number of symbols on the graph) and the reliability of LES data in reproducing the flow statistics are provided in Salizzoni *et al.* (2023).

In the case of light releases ($\rho_s/\rho_0 = 0.2; 0.4$) most of the variations of both coefficients γ_m and δ_m occur within 10 source radii (see figure 5), attaining peak values that exceed significantly those for an iso-density jet. Their influence on the production and shape terms of α_E is however weighted by the local value of the density ratio ρ_m/ρ_0 (see Eq. 3.1). This implies that, even if γ_m and $-\delta_m$ increase with z more rapidly for a light jet than for an iso-density jet (see figure $5a-c$), the evolution of α_{prod} is very similar. At the same time, α_{shape} varies very little and is close to 0 for the light jet further than $10r_s$, indicating no changes to the shape of the profiles. As a result, and as already evidenced by Salizzoni *et al.* (2023), the evolution of the entrainment coefficient $\alpha_E = \alpha_{prod} + \alpha_{shape}$ for the light jet is not markedly different from that of an iso-density jet. In both cases of a light and iso-density jet, α_{prod} rapidly becomes the most significant contribution to the global entrainment.

The heavy jet cases, i.e. $\rho_s/\rho_0 = 1.5; 5; 10$, behave differently (see figure $5d-f$). The contribution of the shape term α_{shape} decreases much more slowly and is not negligible

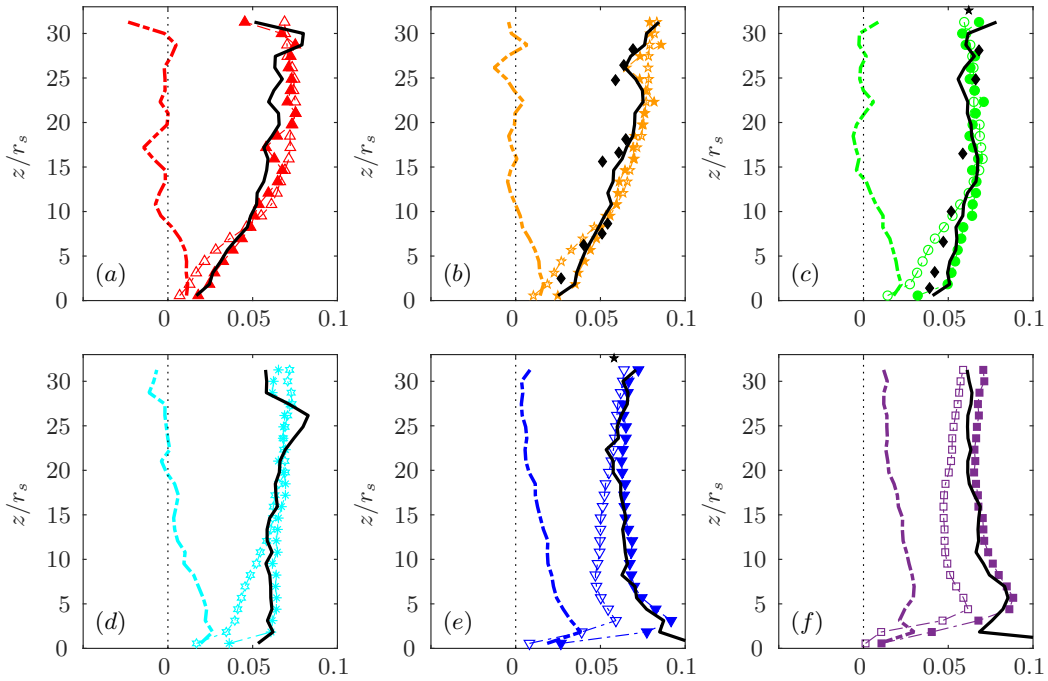


FIGURE 6. Vertical evolution of the entrainment coefficients α (solid black lines), α_E (filled symbols), α_{prod} (open symbols) and α_{shape} (dashed lines), for light jets (a,b), iso-density jet (c) and the 3 heavy jets (d-f). Also shown: experimental data of Salizzoni *et al.* (2023) represented by black diamonds in (b) and (c) and Charonko & Prestridge (2017) (black pentagrams) in (c) and (e).

within almost the whole computational domain. In the very near field ($z \leq 5r_s$), due to the high value of α_{shape}, the entrainment coefficient is clearly enhanced compared to that of an isodensity jet. When $z \geq 5r_s$, α and α_E follow the same trend as α_{shape} i.e. a slight decrease, then they reach a value close to $\alpha_0 \approx 0.07$, which is in close agreement with the estimate provided by direct numerical simulations on isodensity jets (van Reeuwijk *et al.* 2016). The production term for heavy jets is instead reduced in the very near field ($z \leq 4r_s$) due to the reduced TKE production.

It is clear from the analysis above that the evolution of the profile coefficients and entrainment contributions depend strongly on the density ratio and its distance to the source. In order to obtain a clearer picture of the effect of the density ratio, we remove the near-source region $z/r_s < 15$ from the analysis, as this region (for the case of the heavy releases) is strongly affected by the breakdown of the potential core, which implies strong contributions to α_{shape}. As can be seen in figure 6, this discards contributions of α_{shape} in all except the heaviest cases. Even with the removal of data for $z/r_s < 10$, the range of density ratios remains considerable and spans $0.5 < \rho_m/\rho_0 < 4$.

When plotting γ_m and $-\delta_m$ as a function of the density ratio ρ_m/ρ_0, all simulations draw clear one-to-one dependencies of the two coefficients on the density ratio (figure $7a-b$), which are well fitted by a power-law with exponents -0.17 and -1.4 for γ_m and δ_m, respectively. Also plotted in these figures are the experimental results by Salizzoni *et al.* (2023) for a light jet ($\rho_s/\rho_0 = 0.4$) and an iso-density jet, and estimates inferred from the experiments by Charonko & Prestridge (2017) for a heavy jet. Even though distributed over a narrower range of values of ρ_m/ρ_0, the experimental results correspond closely to

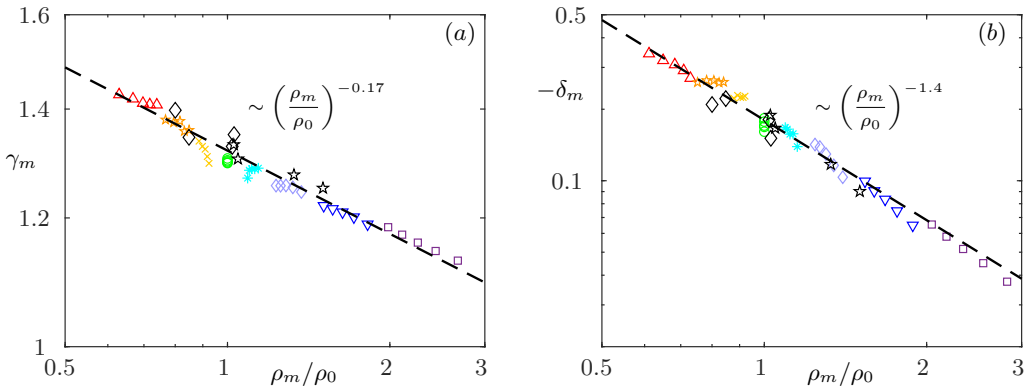


FIGURE 7. Log-log plot of the profile coefficients γ_m (a) and $-\delta_m$ (b) as a function of the density ratio. Symbols as in figure 3. Black pentagrams: Charonko & Prestridge (2017). Black diamonds: Salizzoni *et al.* (2023). Dashed lines represent power-law behaviours with slopes -0.17 for γ_m (a) and -1.4 for δ_m (b).

the numerical data, confirming that the descending trends of γ_m and $-\delta_m$ with ρ_m/ρ_0 observed here are a robust feature of these flows.

Finally, we show in figure 8 the dependence of α on ρ_m/ρ_0 for all simulations (over the range $10 < z/r_s < 30$) and including the experimental estimates by Salizzoni *et al.* (2023) and Charonko & Prestridge (2017). The black dashed line shows the prediction of $\alpha \approx \alpha_{prod}$ based on the power-law scaling observed in figure $7a-b$, indicating a decreasing trend with a much smaller exponent than those for γ_m and δ_m. Indeed, $\alpha_{prod} = (\rho_m/\rho_0)\delta_m/(2\gamma_m)$, and $\delta_m/\gamma_m \sim \rho_m/\rho_0^{-1.23}$ (see figure 7), implying that $\alpha_{prod} \sim \rho_m/\rho_0^{-0.23}$, i.e. only very weakly dependent on ρ_m/ρ_0. This slight decreasing trend is lost when taking into account the contribution of α_{shape}. Although the data range is too limited to make definite statements, no clear dependence of α on the density ratio is discernible.

Figure 8 also shows (red solid line) the relation provided by the R&S scaling (1.2), which is evidently not in accordance with the numerical and experimental data. To get insight on the mismatch between the data and the R&S scaling, we can investigate the latter's validity by manipulating the entrainment relation (3.1). According to (3.1), a sufficient condition for the R&S result $\beta = 1/2$ to hold is for the TKE energy production to scale as $\alpha_{prod} \sim (\rho_m/\rho_0)^{1/2}$ and the contribution of the shape term α_{shape} to be negligible.

Although the shape term α_{shape} vanishes for the light jets, this is not the case for the heavy jets, which are instead characterised by a persistent potential core, whose extent increases for increasing density ratios. In the case of heavy releases, it is therefore evident that density differences affect the flow in several distinct respects that are likely to be difficult/impossible to decouple in the near field.

If self-similarity had to be recovered, therefore, this would be only for low-density releases, given their tendency to squeeze the potential core in few source radii. Similarity solutions should however be consistent with the evolution of α_{prod}, whose scaling, determined here based on empirical evidence, goes as $(\rho_m/\rho_0)^{-0.23}$, i.e. different from that initially suggested by R&S. Strictly speaking, this power-law behaviour of α_{prod} with density ratio may not be valid outside the range of density ratios studied.

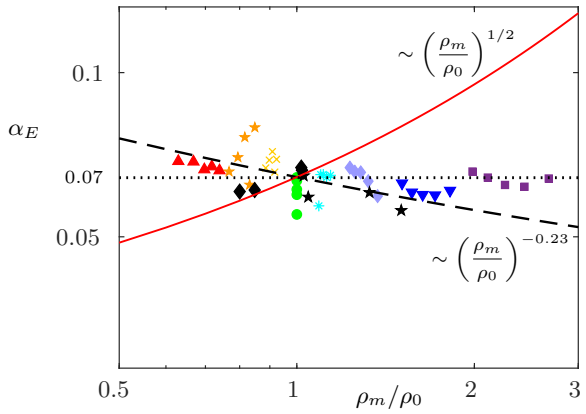


FIGURE 8. Entrainment coefficient as a function of the density ratio. Symbols as in figure 3 and 7. Shown in the black diamonds are the experimental data of Salizzoni *et al.* (2023) and in the black stars the experimental data by Charonko & Prestridge (2017). The black dotted line is showing $\alpha = 0.07$, the dashed black line represents the power-law behaviour of α_{prod}, while the solid red line represents the R&S scaling for α (i.e. Equation 1.2, with $\alpha_0 = 0.068$).

6. Conclusions

We studied the effect of a variable density ρ_m on the turbulent entrainment of ambient fluid, of density ρ_0, within axi-symmetric jets, focusing on the evolution of the entrainment coefficient α and its dependence on the density ratio ρ_m/ρ_0.

Early laboratory experiments conducted by R&S quantified entrainment in the far field of variable-density jets and suggested a scaling described by $\alpha \propto (\rho_m/\rho_0)^{1/2}$. However, recent experimental and numerical analyses that focused on jet's near field (Salizzoni *et al.* 2023) have challenged this scaling. In order to address this apparent contradiction, we revisited the original experimental data by R&S in §2. We demonstrated that, since the R&S experiments focused on the far-field behaviour of the jet, their data does not provide sufficient evidence for a definitive conclusion about the dependence of α on ρ_m/ρ_0.

To investigate the scaling of α on ρ_m/ρ_0, we performed large-eddy simulations, verified against experimental data for two reference cases (Salizzoni *et al.* 2023), of jets having a density at the source varying over two orders of magnitude. Following Salizzoni *et al.* (2023), the interpretation of the results relies on the entrainment decomposition by van Reeuwijk & Craske (2015), whose formulation was conveniently extended to deal with large density releases. This framework allows the entrainment coefficient to be expressed as a function of two integral quantities, γ_m and δ_m expressing the effect of a varying shape of the mean radial velocity profiles and that of the TKE production, respectively. Numerical results show that an increasing density ratio (ρ_m/ρ_0) has a major effect in reducing both γ_m and δ_m. This tendency is in very good agreement with that depicted by recent experimental data, obtained over a narrower rage of ρ_m/ρ_0. These modifications reflect the tendency of heavier releases to delay, compared to the lighter ones, the TKE production and therefore the modification of the radial profiles of the mean velocity. Despite this, their combined effect in the overall entrainment process tends to cancel, so that the entrainment coefficient turns out to be relatively insensitive to variations of the density ratio (ρ_m/ρ_0).

Our observations are, therefore, not consistent with the scaling $\alpha \sim (\rho_m/\rho_0)^{1/2}$ originally proposed by R&S. This has significant implications for the mathematical modelling of variable-density jets, since the R&S entrainment relation is indeed the only one consis-

tent with full self-similarity of the flow (for similarity solutions see, for example, Van den Bremer & Hunt 2010). Therefore, our findings suggest that variable-density jets are not expected to be self-similar in those (typically near-field) parts of the flow where the effects of large density differences are significant.

However, the simulations also clearly show that variable-density effects on entrainment are compounded by entrance effects, particularly the existence of a potential core. We showed that the length of the potential core has a strong dependence on the density ratio, which, in turn, has a direct effect on the profile coefficient γ_m which affects α. Entrance effects cannot be expected to have any universality since they are intimately related to the manner in which the fluid is injected into the domain and will therefore be configuration-specific. For this reason, it will be challenging to make further progress regarding the scaling of α without resorting to idealised simulations. One way to circumvent the potential-core issue is to perform variable-density simulations of a planar temporal jet (e.g. Cimarelli *et al.* 2021). For this flow, the jet evolves in time rather than in space, and it will be possible to study the dependence of α on the density ratio once the initial transients have passed.

In a more general way, there is a clear need for further experimental and numerical work on variable-density releases covering a large range of source conditions. This is required to widen our knowledge on the dynamics of these flows, both in case of momentum-dominated releases (variable-density jets) and buoyancy-dominated releases, usually referred in the literature as non-Boussinesq plumes (Rooney & Linden 1996; Woods 1997; Lanzini *et al.* 2024).

Acknowledgements

MvR acknowledges financial support of the Engineering and Physical Sciences Research Council (EPSRC) through the project Multi-scale dynamics at the turbulent/non-turbulent interface of jets and plumes grant EP/R042640/1.

Declaration of interests

The authors report no conflict of interest.

REFERENCES

Ai, J., Law, A. W.-K. & Yu, S. C. M. 2006 On Boussinesq and non-Boussinesq starting forced plumes. *J. Fluid Mech.* **558**, 357–386.

Amielh, M., Djeridane, T., Anselmet, F. & Fulachier, L. 1996 Velocity near-field of variable density turbulent jets. *Int. J. Heat Mass Transfer* **39** (10), 2149–2164.

Van den Bremer, T. S. & Hunt, G. R. 2010 Universal solutions for Boussinesq and non-Boussinesq plumes. *J. Fluid Mech.* **644**, 165–192.

Bruneau, C.-H. 2000 Boundary conditions on artificial frontiers for incompressible and compressible Navier-Stokes equations. *Math. Model. Numer. Anal.* **34**, 303–314.

Bruneau, C.-H. & Fabrie, P. 1994 Effective downstream boundary conditions for incompressible Navier-Stokes equations. *Int. J. Numer. Methods in Fluids* **19**, 693–705.

Bruneau, C.-H. & Fabrie, P. 1996 New efficient boundary conditions for incompressible Navier-Stokes equations: a well-posedness result. *Math. Model. Numer. Anal.* **30**, 815–840.

Charonko, J. & Prestridge, K. 2017 Variable-density mixing in turbulent jets with coflow. *J. Fluid Mech.* **825**, 887–921.

Cimarelli, A., Mollicone, J.-P., van Reeuwijk, M. & De Angelis, E. 2021 Spatially evolving cascades in temporal planar jets. *J. Fluid Mech.* **910**, A19.

Craske, J., Salizzoni, P. & van Reeuwijk, M. 2017 The turbulent Prandtl number in a pure plume is 3/5. *J. Fluid Mech.* **822**, 774–790.

Djeridane, T., Amielh, M., Anselmet, F. & Fulachier, L. 1996 Velocity turbulence properties in the nearfield region of axisymmetric variable density jets. *Phys. Fluids* **8** (6), 1614–1630.

Ezzamel, A., Salizzoni, P. & Hunt, G. R. 2015 Dynamic variability of axisymmetric buoyant plumes. *J. Fluid Mech.* **765**, 576–611.

García-Villalba, M., Fröhlich, J. & Rodi, W. 2006 Identification and analysis of coherent structures in the near field of a turbulent unconfined annular swirling jet using Large Eddy Simulation. *Phys. Fluids* **18** (5), 055103.

Gerashchenko, S. & Prestridge, K. 2015 Density and velocity statistics in variable density turbulent mixing. *J. Turbul.* **16** (11), 1011–1035.

Gharbi, A., Amielh, M. & Anselmet, F. 1995 Experimental investigation of turbulence properties in the interface region of variable density jets. *Phys. Fluids* **7** (10), 2444–2454.

Gharbi, A., Ruffin, E., Anselmet, F. & Schiestel, R. 1996 Numerical modelling of variable density turbulent jets. *Int. J. Heat Mass Transfer* **39** (9), 1865–1882.

Jarrin, N., Benhamadouche, S., Laurence, D. & Prosser, R. 2006 A synthetic-eddy-method for generating inflow conditions for large-eddy simulations. *Int. J. Heat Fluid Flow* **27** (4), 585–593.

Jiang, L., Creyssels, M., Hunt, G. R. & Salizzoni, P. 2019 Control of light gas releases in ventilated tunnels. *J. Fluid Mech.* **872**, 515–531.

Kaminski, E., Tait, S. & Carazzo, G. 2005 Turbulent entrainment in jets with arbitrary buoyancy. *J. Fluid Mech.* **526**, 361.

Lanzini, S., Marro, M., Creyssels, M. & Salizzoni, P. 2024 Helium plumes at moderate reynolds number. *Phys. Rev. Fluids* **accepted**.

Mehaddi, R., Boulet, P., Koutaiba, M., Vauquelin, O. & Candelier, F. 2021 Emptying-filling boxes with non-boussinesq plumes and fountains. *Phys. Rev. Fluids* **6**, 083801.

Morton, B. R. 1965 Modeling fire plumes. *Tenth Symposium (International) on Combustion* pp. 973–982.

Morton, B. R., Taylor, G. I. & Turner, J. S. 1956 Turbulent gravitational convection from maintained and instantaneous sources. *Proc. Roy. Soc. London A* **234**, 1–23.

O'Hern, T. J., Weckman, E. J., Gerhart, A. L., Tieszen, S. R. & Schefer, R. W. 2005 Experimental study of a turbulent buoyant helium plume. *J. Fluid Mech.* **544**, 143–171.

Panchapakesan, N. R. & Lumley, J. L. 1993 Turbulence measurements in axisymmetric jets of air and helium. Part 2. Helium jet. *J. Fluid Mech.* **246**, 225–247.

Papanicolaou, P. N. & List, E. J. 1988 Investigations of round vertical turbulent buoyant jets. *J. Fluid Mech.* **195**, 341–391.

Pietri, L., Amielh, M. & Anselmet, F. 2000 Simultaneous measurements of temperature and velocity fluctuations in a slightly heated jet combining a cold wire and laser doppler anemometry. *Int. J. Heat Fluid Flow* **21** (1), 22–36.

Priestley, C. H. B. & Ball, F. K. 1955 Continuous convection from an isolated source of heat. *Quart. J. Roy. Met. Soc.* **81** (348), 144–157.

van Reeuwijk, M. & Craske, J. 2015 Energy-consistent entrainment relations for jets and plumes. *J. Fluid Mech.* **782**, 333–355.

van Reeuwijk, M., Salizzoni, P., Hunt, G.R. & Craske, J. 2016 Turbulent transport and entrainment in jets and plumes: A DNS study. *Phys. Rev. Fluids* **1**, 074301.

Ricou, F. P. & Spalding, D. B. 1961 Measurements of entrainment by axisymmetrical turbulent jets. *J. Fluid Mech.* **11**, 21–32.

Rooney, G. G. & Linden, P. F. 1996 Similarity considerations for non-Boussinesq plumes in an unstratfied environment. *J. Fluid Mech.* **318**, 237–250.

Salizzoni, P., Vaux, S., Creyssels, M., Amielh, M., Pietri, L. & Anselmet, F. 2023 Turbulent transfer and entrainment in a low-density jet. *J. Fluid Mech.* **968**, A27.

Vauquelin, O. 2015 Oscillatory behaviour in an emptying filling box. *J. Fluid Mech.* **781**, 712–726.

Vaux, S., Mehaddi, R., Vauquelin, O. & Candelier, F. 2019 Upward versus downward non-Boussinesq turbulent fountains. *J. Fluid Mech.* **867**, 374–391.

Viggiano, B., Dib, T., Ali, N., Mastin, L. G., Cal, R. B. & Solovitz, S. A. 2018 Turbu-

lence, entrainment and low-order description of a transitional variable-density jet. *J. Fluid Mech.* **836**, 10091049.

Vreman, A. W. 2004 An eddy-viscosity subgrid-scale model for turbulent shear flow: Algebraic theory and applications. *Physics of Fluids* **16** (10), 3670–3681.

Wang, H. & Law, A.W-K. 2002 Second-order integral model for round turbulent jet. *J. Fluid Mech.* **459**, 397–428.

Wang, P., Frohlich, J., Michelassi, V. & Rodi, W. 2008 Large-eddy simulation of variable-density turbulent axisymmetric jets. *Int. J. Heat Fluid Flow* **29** (3), 654–664.

Woods, A. W. 1997 A note on non-Boussinesq plumes in an incompressible stratified environment. *J. Fluid Mech.* **345**, 347–356.